Applications of saturable absorption-based nonlinear vertical-cavity semiconductor devices for all-optical signal processing

Claudio Porzi[1], Mircea Guina[2], Nicola Calabretta[3],
Antonella Bogoni and Luca Poti'[3]
[1] *Scuola Superiore Sant'Anna, Pisa*
Italy.
[2] *Optoelectronics Research Centre, Tampere University of Technology, Tampere*
Finland
[3]*COBRA Research Institute, Eindhoven University of Technology, Eindhoven*
The Netherlands.
[3] *Consorzio Nazionale Interuniversitario per le Telecomunicazioni, Pisa*
Italy

1. Introduction

Modern ultrahigh bandwidth optical communication networks create a demand for devices with ever higher performance, conjugating high operation speed, reduced fabrication costs, compactness, and advanced functionality. Passive nonlinear devices based on semiconductor quantum wells (QWs) are promising candidates for many all-optical signal processing (AOSP) applications, that will be described in this chapter. A semiconductor quantum well is formed by a thin layer (typical thickness is ~10 nm) of a semiconductor material placed between two other layers of a second semiconductor material, the middle layer having a smaller band-gap energy than the external layers. Carriers are thus confined in one dimension within the smaller band-gap layer, leading to important modifications of the electronic and optical properties (e.g. higher and discrete density of states for carriers compared to bulk structure). Such QWs are usually arranged in a periodic fashion, with the basic structure alternating several times to form a multiple quantum well (MQW) heterostucture whose optical features can be controlled by the number of QWs. Semiconductor QWs can be fabricated with precise control of layers thickness using standard epitaxial growth techniques like molecular beam epitaxy (MBE) or metal-organic chemical vapour deposition (MOCVD). For applications in the field of optical communications, the material band-gap should fit the desired operating wavelength. By using compounds with different compositions, the energy gap can be adjusted. The III-V compounds (i.e., elements from column III and V of the periodic table) enable operating wavelengths in the three fiber-optic communication bands at 0.85 µm, 1.3 µm and 1.55 µm to be used. The use of QWs has brought many benefits for the development of a large variety of optical telecom devices, such as laser diodes (LDs), semiconductor optical amplifiers (SOAs), electroabsorption modulators (EAMs) and saturable absorbers (SAs). Generally speaking, it is possible to differentiate these devices into two classes, *active* and *passive*. Passive devices differ from active devices in that carriers are not injected into the material (typically by applying an electrical current) to provide optical gain like in LDs or SOAs. Passive devices are therefore usually simpler to fabricate, and require lower overall operating powers than active devices. Typically, passive MQW-based devices exploit the change in light absorption provided by the semiconductor structure under an applied electrical or optical control signal. Change of light absorption within MQWs in the presence of an electric field is due to the quantum-confined Stark effect (QCSE) (as opposed to the weaker Franz-Keldysh effect in bulk materials). On the other hand, the phenomenon responsible for the saturation of absorption under an applied optical field in quantum-confined structures is known as phase-space-filling (in bulk materials one usually refers to the band-filling effect). The optical saturation of absorption is a consequence of the fact that the available states for the electrons and holes are filled by the free carriers generated by the applied optical field. Thus, for low values of incident intensity, photons experience (relatively) high absorption losses, whereas at high intensity values the absorption is saturated, and the material becomes, ideally, transparent. The QCSE is the basis of operation for EAMs, whereas the optically induced saturation of absorption is exploited in SAs. When the absorber is coupled with a mirror on one side (typically a high-reflectivity semiconductor Bragg mirror grown on a substrate), these devices are referred to as semiconductor saturable absorber mirrors (SESAMs), when they are used for mode-locking of ultrafast lasers (Keller et al., 1996), or asymmetric Fabry-Pérot (AFP) etalons/modulators when they are used for signal processing applications (Loka et Smith, 1998). The non-linear phenomenon of saturable absorption can be greatly enhanced by placing the semiconductor MQWs at the antinodes of the vertical Fabry-Pérot cavity formed between the high-reflective semiconductor mirror and the top surface mirror; typically, a vertical-cavity architecture is realized by growing the absorbing layer on a high reflectivity (~ 100%) bottom semiconductor Bragg mirror and finishing the structure with a partially reflective (< 100%) semiconductor or dielectric mirror. Vertical-cavity technology offers a simplification of the device fabrication, versatility in coupling with optical fibres, increased functionality, polarization independence, and most importantly, low switching powers and a high switching contrast. Indeed, due to the cavity effect, the energy that must be applied to the device in order to saturate the nonlinear medium is much lower than the saturating energy of the bare SA, resulting in a decreased "effective" saturation power. Furthermore, the cavity can be designed in such a way that the optical field reflected from the cavity can be totally cancelled when the gate is in the *OFF* state, allowing the normal SA characteristic to be enhanced, and high *ON/OFF* contrast ratio *(CR)* values to be achieved. This concept has been exploited to realize high-contrast EAMs (Yan et al., 1991) and for nonlinear optical processing, in applications for noise suppression for signal regeneration (Isomaki et al, 2003; Massoubre et al., 2006), all-optical switching (Takahashi et al., 1996; Loka et Smith, 1998) and wavelength conversion (Burr et al., 2003; Akiyama et al., 1998). However, the design parameters of the nonlinear AFP cavity can also be tailored to provide a specific target value of the device reflectivity for a given value of the input signal energy which is not necessarily associated with a low-energy photon flux. This allows the application field of nonlinear vertical-cavity semiconductor devices for AOSP to be widened.

In this chapter we review a device engineering method we have developed to provide high functionality of passive nonlinear vertical-cavity devices exploiting saturable absorption in semiconductor MQWs. Section 2 is concerned with the design and fabrication of the vertical-cavity nonlinear gate. The advantages of the proposed approach for all optical gating in terms of enhanced throughput, increased optical signal-to-noise ratio (OSNR), and high switching *CR* are then discussed in Section 3. Subsequently, a specific application in a wavelength conversion experiment is presented in Section 4, whereas in Section 5 and Section 6 we show how this approach enables complex functions for all optical networking and different logic operations, respectively, to be implemented which would not otherwise be possible with standard SAs. Analytical and numerical modelling of devices will be presented throughout the different sections; the models can be exploited for device optimization and design trade-offs. Finally, these results will be summarized in Section 7.

2. Device Structure

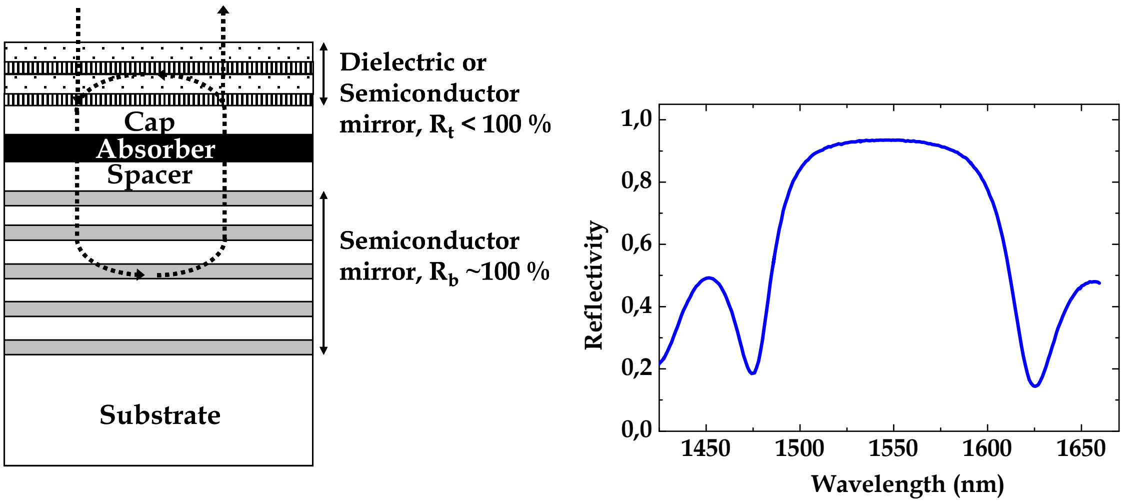

Fig. 1. Left: schematic structure of a nonlinear VCSG based on saturable absorption in MQWs. Right: typical spectral reflectivity of the bottom DBR mirror.

The typical structure of a nonlinear vertical-cavity device based on saturable absorption in semiconductor MQWs is shown in Fig. 1 (left). We will refer to this generic structure throughout the text as a vertical-cavity semiconductor gate (VCSG). The structure consists of an AFP cavity formed between a bottom mirror, with a reflectivity R_b, approaching 100%, and a top mirror with lower reflectivity, R_t. The mirrors can be fabricated based on either semiconductor or dielectric materials or, in the case of the highly reflective bottom mirror, with a thin layer of silver or gold. Saturable losses in the cavity are usually provided by semiconductor QWs (quantum dots or any other medium exhibiting intensity-dependent saturable losses could be used as well). For the experiments presented in the next sections all the samples were grown by solid-source MBE on n-type InP (100) substrate. The samples comprised of a Burstein-Moss shifted distributed Bragg reflector (DBR) with 19.5 pairs of $\lambda/4$ n^+-$Ga_{0.47}In_{0.53}As$/InP, an InP spacer layer, the active region, and a 50-nm InP cap layer (Xiang et al., 2001). The length of the spacer layer varied for different samples depending on the specific target application. The active regions were always comprised of four groups of seven 9-nm-thick $Ga_{0.47}In_{0.53}As$ QWs and 10-nm-thick InP barriers. Each group of QWs has been centered at the antinodes of the 3λ/2 cavity defined between the semiconductor DBR and top surface of the gate. The DBR reflectivity was over 96% in the wavelength range from 1.525 to 1.610 nm. The measured DBR reflectivity spectrum is also shown in Fig 1 (right). In order to decrease the absorption recovery time, the samples were irradiated with I^+ ions with a dose of $5x10^{11}$ cm^{-2} and an energy of 12-MeV.

3. Device Operation

The reflectivity of the generic structure shown in Fig. 1 (left) can be calculated by using the standard formula for an FP cavity incorporating losses (Siegman, 1984). If the resonator has a loss per pass of *(1-exp[-αd])*, α [m^{-1}] being the absorption coefficient of the MQW section, and d [m] its physical length, the reflectivity of the structure in Fig. 1 is given by:

$$R = \frac{\left[\sqrt{R_t} - \sqrt{R_b}\exp(-\alpha d)\right]^2 + 4\sqrt{R_t}\sqrt{R_b}\exp(-\alpha d)\sin^2(\phi_{sp})}{\left[1 - \sqrt{R_t}\sqrt{R_b}\exp(-\alpha d)\right]^2 + 4\sqrt{R_t}\sqrt{R_b}\exp(-\alpha d)\sin^2(\phi_{sp})} \qquad (1)$$

Where ϕ_{sp} is the single-pass phase change of a wave travelling in the structure. The typical spectral reflectivity of an uncoated (i.e. without the top mirror) sample is shown in Fig. 2. The side oscillations that can be observed in the figure are due to the effect of the bottom DBR mirror whereas the dip in the central part of the spectrum corresponds to the FP resonance created between the bottom mirror and the Fresnel reflection at the air-semiconductor interface. At resonance, the value of ϕ_{sp} is $m\pi$, where m is an integer.

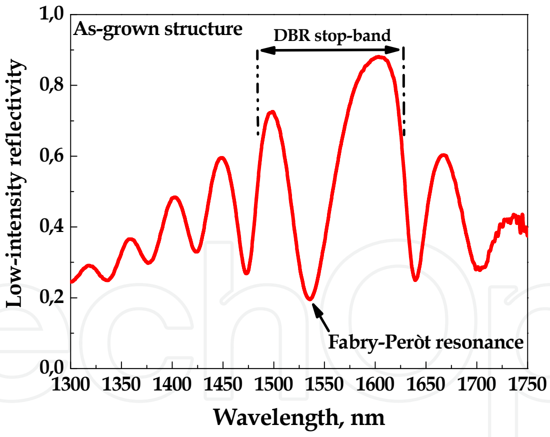

Fig. 2. Low-intensity spectral reflectivity of an uncoated As-grown sample.

The minimum value of reflectivity R_{res} is calculated from (1) as:

$$R_{res} = \left(\frac{\sqrt{R_t} - \sqrt{R_b}\exp(-\alpha \cdot d)}{1 - \sqrt{R_t R_b}\exp(-\alpha \cdot d)}\right)^2 \qquad (2)$$

From the last expression it can be seen that the reflected wave is zero if the top dielectric/semiconductor mirror has a reflectivity satisfying the following condition:

$$R_t = R_b e^{-2\alpha d} \tag{3}$$

The condition expressed by (3) is usually called impedance-matching (IM), and has been widely exploited to realize high-contrast electro absorption modulators or all-optical gates (Yan et al., 1991; Loka et Smith, 1998). By taking into account also the non-saturable part of absorption, α_{ns}, the dependence of α on the energy E_{int} impinging on the medium can be expressed as:

$$\alpha = \alpha_{ns} + \alpha_{sat} = \alpha_{ns} + \frac{\alpha_0}{1 + E_{\mathrm{int}} / E_{sat}}. \tag{4}$$

In (4), α_0 is the unsaturated small-signal absorption coefficient, i.e. the value of the saturable part of absorption, α_{sat}, for applied energies much weaker than the medium saturation energy, E_{sat}. On the other hand, the non-saturable part of the absorption, α_{ns}, which can, for example, be caused by the imperfection of the semiconductor structure, does not change with incident energy.

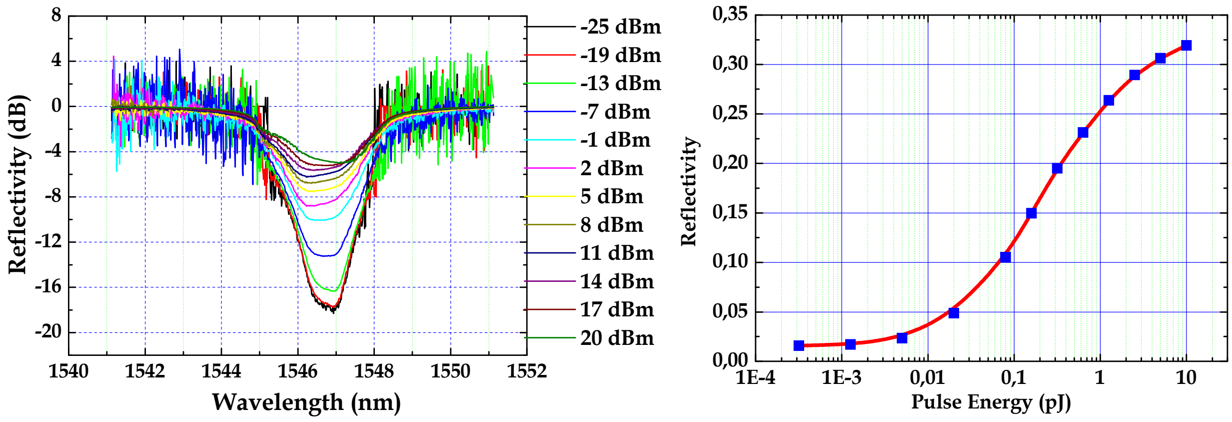

Fig. 3. Left: VCSG spectral reflectivity for different power values of an input pulse tuned at resonance. Right: corresponding nonlinear reflectivity at resonant wavelength.

By substituting (4) into (3) a more general expression for the IM condition can be derived:

$$R_t = R_b e^{-2\left[\alpha_{ns} d + \alpha_0 d / (1 + E / E_{sat})\right]}. \tag{5}$$

In many practical cases, the top mirror reflectivity is designed to satisfy IM condition for low values of the applied optical field, that is for:

$$R_t = R_b e^{-2\left[(\alpha_{ns} + \alpha_0) d\right]}. \tag{5}$$

Under this condition, the typical SA characteristic (i.e. low throughput at low input intensity and high throughput at high input intensity) is strongly enhanced. Measured spectral reflectivity for a VCSG designed to meet the IM condition at low values of input energies and the corresponding nonlinear reflectivity curve at resonance are shown in Fig. 3. By exploiting the dependence of the roundtrip power transmission on the energy incident on the absorber via the nonlinear absorption coefficient α (see eq. 3), one could partially or even totally reverse the nonlinear characteristic of Fig. 3 (right). It can indeed be deduced from (5) that, for a given R_t, the IM condition can be satisfied for a particular value of the signal energy, provided that R_t is higher than the roundtrip power transmission associated with unsaturated absorption, i.e. for:

$$R_t > R_b e^{-2[(\alpha_{ns}+\alpha_0)d]}. \tag{7}$$

When (7) holds, the cavity impedance can still be matched by using an input optical field that partially saturates the absorption to satisfy the condition given by (3), with α being the general, intensity-dependent expression of (4). In order to distinguish it from the usual case in which the IM is achieved for weak values of the applied field, we will refer hereafter to a structure designed to satisfy the generic condition given by (7) as an *impedance-detuned* VCSG.

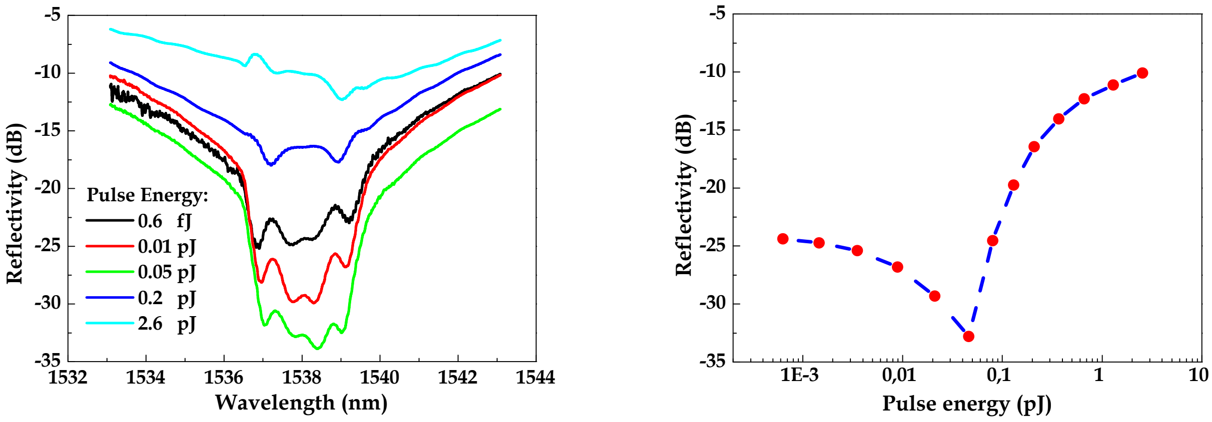

Fig. 4. Left: impedance-detuned VCSG spectral reflectivity for different values of energies of an input pulse tuned at resonance. Right: corresponding nonlinear reflectivity at resonance.

The typical spectral response and the relative characteristic at resonance of an impedance-detuned VCSG for different energy values of the input signal are shown in Fig. 4. In order to obtain a nonlinear characteristic as that of Fig. 4 (right), the low-intensity reflectivity spectrum for an as-grown (i.e., uncoated) structure was first measured. A top dielectric coating consisting of two layers of SiO_2/TiO_2 was then deposited on the sample, providing a reflectivity of ~ 53%, a value that allowed detuning (from the zero energy point) of the IM energy. The reflectivity spectra of Fig. 4 (left) had a minimum value at the resonance of about -33 dB for an applied pulse energy of -0.05 pJ. Due to detuned impedance, the reflectivity for the lowest input energy (0.6 *fJ)* is about 10 dB higher. When the power of the signal was increased above 0.05 pJ, the saturation of the MQWs absorption increased, resulting in the increased reflectivity. Fig. 4 (right) further clarifies the dependence between the minimum reflectivity at cavity resonance and the input energy. The advantage arising from the use of the *impedance-detuned* design is explained in the following. In many practical applications, the reflectivity exhibited by an applied probe signal incident on the VCSG is changed by an intense optical pump field (see, for example, the scheme of Fig 5 showing a typical wavelength conversion set-up). In order to understand the benefits of the proposed design for practical applications, we will use as figures of merit for the switching capability of the device the *ON/OFF CR* and the eye-opening (*EO*) of the reflected probe signal. The *CR* of a modulated signal is defined as the ratio between its high and low levels; with reference to Fig. (5), the *CR* is then given by:

$$CR = \frac{P_{level1}^{\lambda_2}}{P_{level0}^{\lambda_2}} = \frac{P_{CW}^{\lambda_2} R_{ON}}{P_{CW}^{\lambda_2} R_{OFF}} = \frac{R_{ON}}{R_{OFF}} \tag{9}$$

where R_{ON} and R_{OFF} are the reflectivity values of the gate in the *ON* and *OFF* states, respectively. The converted signal *EO* is given by:

$$EO = P_{level1}^{\lambda_2} - P_{level0}^{\lambda_2} = P_{CW}^{\lambda_2} (R_{ON} - R_{OFF}) \tag{10}$$

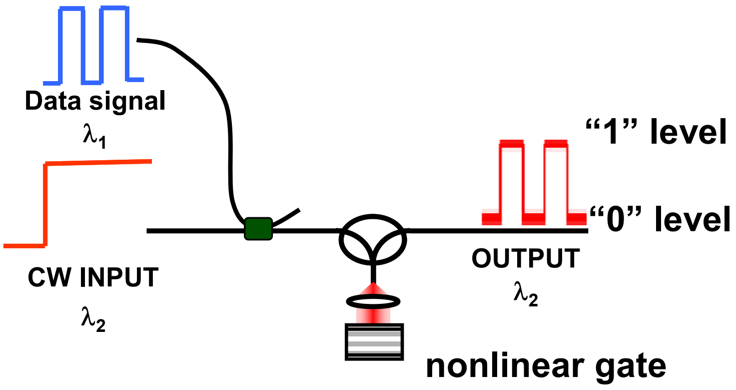

Fig. 5. Schematic of wavelength conversion with VCSG.

The output signal *CR* takes into account the amount of modulation transfer from the data signal onto the CW probe, and a high *CR* (say, at least 10 dB) ensures resilience of the signal to transmission impairments when it has to be launched through an optical transmission channel. On the other hand, the *EO* is related to the power throughput of the gate. A fair throughput is important in order to have a good optical signal-to-noise ratio (OSNR) at the gate output, which makes subsequent optical amplification of the signal without significant degradation possible. Also, a high throughput allows the noise characteristic of the detected signal to be improved at the receiver side. In general, both the *CR* and *EO* (which are related to each other, as can be easily seen from (9) and (10)) have an effect on the properties of the system in terms of the photodetected output signal noise. In digital communications, the systems performance is conveniently expressed in terms of error probability and, in the Gaussian approximation, the receiver sensitivity required to achieve a given bit error rate (BER) depends on the so called Q-factor, given by:

$$Q = \frac{I_1 - I_0}{\delta_1 + \delta_0} \tag{11}$$

where I_1 (I_0) and δ_1 (δ_0) are the mean and standard deviation of the receiver output for a 1 (0) bit, respectively. Clearly, $I_1 - I_0$, is directly proportional to the *EO*. From (11) it can also be seen that decreasing the *CR* leads to an increase of the optical power required at the receiver to attain a given BER (Agrawal, 2002). In general, the receiver performance can be improved by maximizing both the *CR* and the *EO* of the nonlinear gate output signal. In Fig. 6, two possible operating conditions of an optical modulator based of a nonlinear VCSG designed to satisfy the IM condition in the low energy regime are presented.

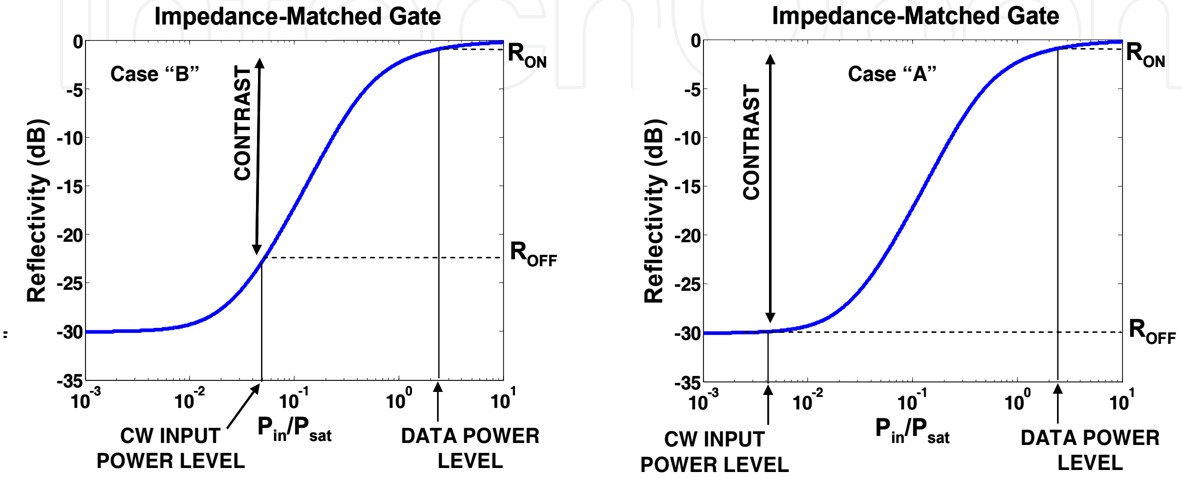

Fig. 6. Left: high CR and limited throughput can be obtained with this configuration. Right: this configuration corresponds to high throughput and low CR of the gate.

In case "A", the CW probe signal is in the low power regime (well below the gate saturation power P_{sat}) whereas the pump signal level is high enough to turn the gate in the *ON* state. A fair *ON/OFF* CR can be achieved with this configuration; however, it is also clear that the power throughput, $P_{CW} \cdot R_{ON}$, and consequently the *EO*, are limited by the low probe signal power level. One could attempt to overcome this limit by increasing the gate saturation power P_{sat}, but clearly this solution would not be beneficial in terms of the required switching power. On the other hand, for case "B" of Fig. 6, the CW probe signal is partially saturating the absorber in the nonlinear gate. This condition describes the situation of an increased throughput (with respect to case "A") at the expense of a reduced *CR*. A trade-off between these two parameters should then be found when operating with the (low-energy) IM design. However, by exploiting the impedance-detuned design it is possible to maximize both parameters, as shown in Fig. 7 (left). By setting the CW probe power to the level that gives the minimum value of reflectivity, a large CR together with an increased throughput (with respect to the case "A" of Fig. 6) can be obtained for the same saturation power. Both figures of merit can then be optimized, regardless of the switching power value, which can hence be kept as low as possible in designing the device (Porzi et al., 2005). As has already been discussed, an impedance-detuned device can be achieved by coating the as-grown structure of Fig. 1 (left) with a top mirror having a reflectivity higher than the roundtrip power transmission value associate with unsaturated absorption, $R_b exp(-2\alpha_0 d)$. The effect of increasing the top mirror reflectivity is shown in Fig. 7 (right); for larger detuning of the impedance, the value of R_{ON} decreases as well due to the unavoidable presence of non-saturable losses, leading to higher values of the gate insertion losses, $(1-R_{ON})$. However, the possibility to shape the nonlinear characteristic is of particular interest for broadening the application fields of nonlinear VCSGs.

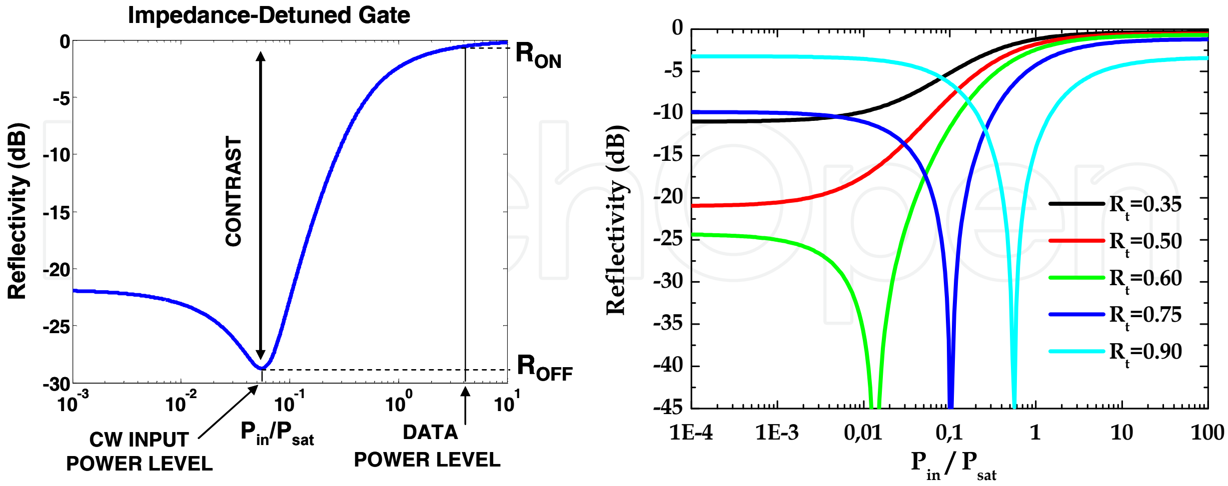

Fig. 7. Left: impedance detuned design: high *CR* and *EO* values can be simultaneously accomplished. Right: nonlinear VCSG characteristic at the resonant wavelength for different values of top mirror reflectivity R_t (other parameters: R_b=100%, $\alpha_0 d$=0.28, $\alpha_{ns}d$=0.01).

4. Broadband wavelength conversion with impedance detuned VCSG

A straightforward application of the MQWs-based nonlinear VCSG is in wavelength conversion, which refers to the modulation transfer from a data signal at a given wavelength onto a CW or clock probe signal at a different wavelength. Wavelength conversion is a key technique for switching and routing in next generation optical communication networks (Brackett et al., 1993), leading to increased network flexibility, throughput, capacity, and efficient solutions to alleviate congestion at network nodes. In order to effectively exploit such a technique in practical applications the quality of the converted signal must be suitable for long distance transmission, which requires a large dynamic *CR* in the converted output. In addition, efficient operation requires low optical input powers for the control signal, and a high power in the converted output. Cross-absorption saturation in semiconductor absorbers have been previously proposed (Burr et al., 2003; Akiyama et al., 1998) to perform wavelength conversion, but their performances were limited due to either poor conversion range or output signal *CR*. The proposed impedance-detuned design allows high switching contrasts and fair gate throughputs to be obtained. Furthermore, this technology allows correct operation over a broad band of input data (i.e. the signal to be converted) wavelengths (Porzi et al., 2006).

4.1 Quasi-static broadband characterization

The reflectivity of a VCSG shows a spectrally dependent behaviour due to its resonant structure. Nevertheless, a locally generated probe signal can be tuned close to a resonant wavelength, whereas the absorption in the QWs due to the broadband excitonic interaction in the proximity of the material band-gap can be saturated by a data pump field tuned away from the resonant wavelength. As a consequence, the reflectivity of the probe signal will be modified as well. In order to investigate the degradation of the gate performance as a function of the optical detuning of pump from resonance, a time-resolved measurement of the *ON/OFF CR* of the wavelength-converted signal for different values of pump-probe detuning was performed. The measurement was carried out in a *quasi-static* condition, by using pump pulses much longer than the carrier recombination time in the absorber medium at a repetition frequency much lower than the absorber recovery rate, to allow complete recovery of absorption between two subsequent pulses. In particular, 8 ns-long pump pulses, at the repetition rate of 10 kHz were applied to the VCSG. The wavelength of the probe signal was set to ~ 1536 nm, where the etalon exhibited a resonance. The wavelength of the pump beam could be varied to provide up to 25 nm of detuning from the cavity resonance.

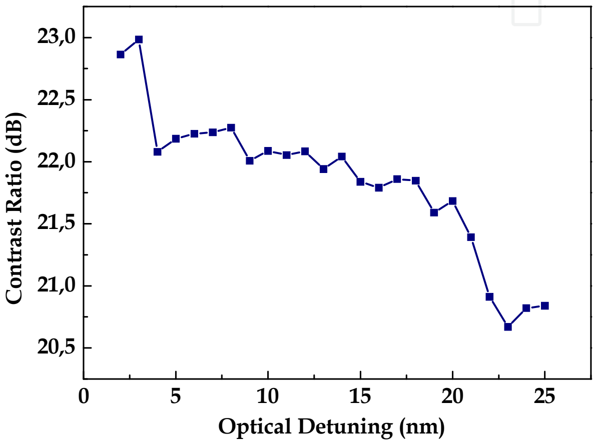

Fig. 8. Probe output extinction ratio as a function of pump detuning.

The power of the probe beam at the VCSG input was set at about -2 dBm in order to match the condition of minimum reflectivity in the absence of pump light. The average pump power was set to 0 dBm at the input of the VCSG for all the values of pump wavelength. The nonlinear characteristic at the resonant wavelength for the device used in the experiment is that of Fig. 4 (right), exhibiting an impedance-detuned feature. The reflected probe signal was photodetected and sent to an oscilloscope; maximum and minimum voltages (V_{max} and V_{min}, respectively) of the detected signal for different pump-probe detuning were stored to calculate the switched output *ON/OFF CR* (in dB), defined as $10log_{10}(V_{max}/V_{min})$. The measured values are shown in Fig. 8 as a function of pump-probe optical detuning. As expected, a maximum *CR* of ~ 23 dB was achieved for low pump-probe detuning (i.e., when the pump light wavelength was close to the cavity resonance), since in this case the pump field distribution is enhanced inside the resonator. However, the device exhibits a rather flat response over a wide range of pump wavelengths and the CR degradation remains below ~ 2.5 dB over 25 nm of pump detuning from resonance. The absolute value for the *CR* in this experiment is set by the value of pump light switching energy (which corresponded to a pump intensity on the absorber as low as ~ 1.5 kW/cm^2).

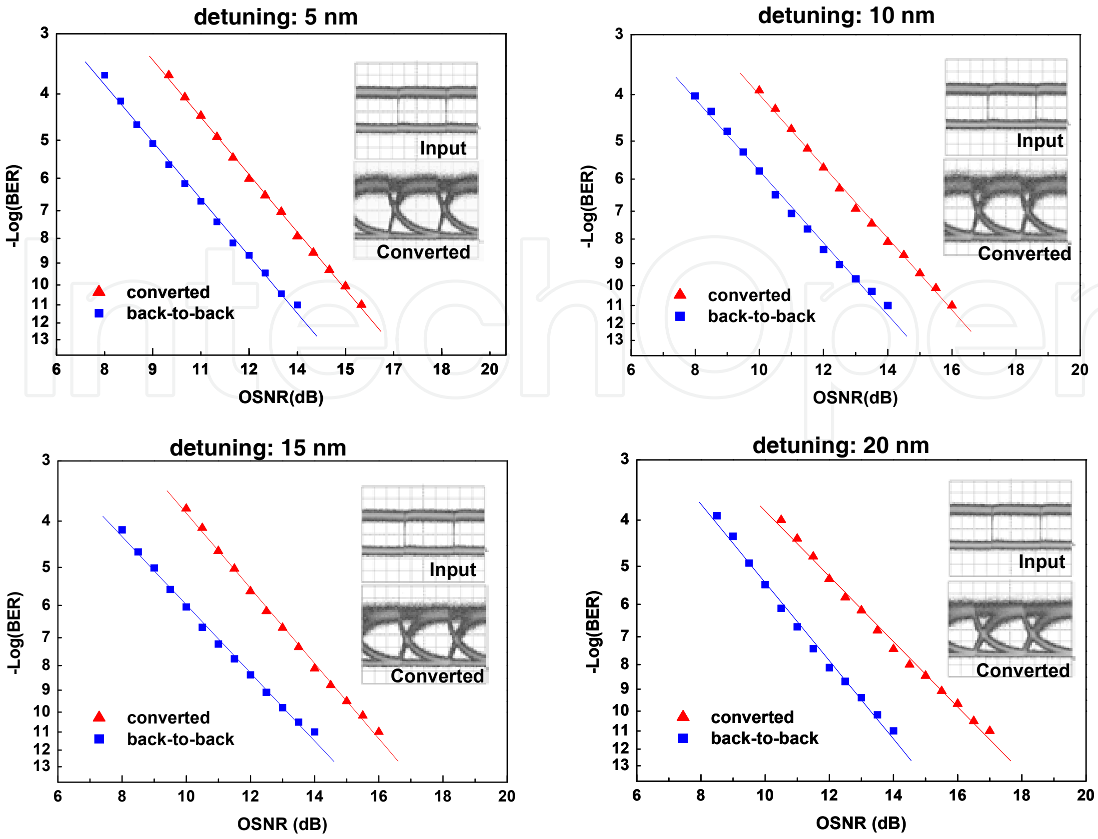

Fig. 9. BERvsOSNR for the converted probe light (triangles) and the input data (circles) for different pump-probe optical detuning.

4.2 Wavelength conversion experimentt

For the wavelength conversion experiment the pump light was modulated by means of a Mach-Zehnder (MZ) modulator driven by a 2^{31}-1 Pseudo-Random Bit Sequence (PRBS). The probe CW signal was set at resonance with a power level satisfying the IM condition, as in the previous case. After selecting the reflected probe light from the gate by means of optical filters, a standard optically amplified receiver was used in order to perform BER measurements of the converted data as a function of OSNR. Also, a wide-bandwidth (50 GHz) sampling oscilloscope was used to monitor the eye diagram of the wavelength-converted data. In this experiment the data repetition rate was limited by the carrier recombination time in the absorber, which was previously measured with a pump-probe technique to be ~500 ps. Nevertheless, error-free operation was observed for data rates up to 2 Gb/s. However, in order to investigate the performance of the VCSG-based wavelength converter in terms of conversion bandwidth, and avoid degradation of the converted data due to carrier recombination effects, the repetition rate of the input data was set at 622 Mb/s. In the past years, several reports of semiconductor saturable absorbers with a response below 1 ps have been reported (Delpon et al., 1998; Takahashi et al. 1996). Thus, by increasing the ion-irradiation dose, the operation speed of the VCSG-based wavelength converter could be easily increased up to the multi-GHz regime. The results of BER vs. OSNR measurements for values of pump-probe detuning of 5, 10, 15 and 20 nm are shown in Fig. 9, together with the relative pump data back-to-back BER curves. The OSNR penalty, with respect to the back-to-back values, is limited to ~ 2.5 dB for all the measurements. The

VCSG input pump powers in the experiments ranged from ~ 6 dBm, at the lowest values of pump-probe detuning, up to ~ 8 dBm for the highest value of detuning. These values corresponded to an optimized eye diagram for the converter output data. With these values of pump input powers, the corresponding converted average power at the VCSS output ranged from ~ -18 dBm to ~ -16 dBm. The converted output power was limited by the pump power levels and by the butt-coupling losses for the back-reflected light from the VCSG. The probe output power when pump was switched off was ~ -35 dBm.

5. Signal processing with VCSG for all-optical packet switching

In this section, self-induced effects in VCSG are discussed, i.e. the case in which the nonlinear reflectivity changes are induced by the signal itself, rather than by an additional control beam as in the case of wavelength conversion. This feature can be useful to realize several functionalities which are required in packet switched networks. In particular, the implementation of an optical header extractor and of an optical seed pulse extractor will be discussed in this section. Optical packet switching (OPS) and optical burst switching (OBS) offer fast dynamic allocation of optical channels, with bandwidth occupation only when the data are actually transmitted, leading to an efficient usage of the available resources. For this scope, an optical header has to be inserted before the data, which is sent in the form of payload packets; the optical header contains information on payload destination. The core functionality of an optical switch is to selectively transmit packets from a particular input port to a particular output port, according to the header routing information. Thus, extraction of the packet header is required at the input interface of the packet switch. Several all-optical header extraction (AO-HE) and processing techniques have been considered and demonstrated in the recent years. The header information could be transported either by using an in-band header section having the same wavelength as the payload data, by using different wavelengths for the header and the payload section, or by using an orthogonal modulation format for the header. In the case of in-band transmission, the header can either have the same modulation format of the payload data or a different one. Among the different techniques for coding an in-band transmitted header, pulse position coding (PPC) is attractive due to its simple implementation. In PPC an optical header is uniquely defined by the time distance between two on-off-keying (OOK) modulated pulses. PPC allows simple header recognition by using a self-correlation technique which does not need generation of header reference patterns in the header recognition block (Calabretta et al., 2001). Another useful functionality for OPS networks is all-optical seed pulse extraction (AO-SPE) from the incoming packets, which is needed for synchronization of different inputs of a switch node in time-slotted operation. By exploiting self-induced effects in nonlinear optical devices, asynchronous AO-HE and AO-SPE can be achieved. SOAs have been widely exploited to implement AO-HE and AO-SPE (Calabretta et al., 2004; Vegas Olmos et al., 2005; Huang et al., 2005). We demonstrate in this section both AO-HE and AO-SPE functionalities by exploiting the flexibility in designing the nonlinear characteristic of a VCSG (Porzi et al., 2007). Self-induced effects in VCSG provide important benefits compared with other all-optical techniques in terms of efficiency, power consumption and polarization dependency. For example, the VCSG preserves the compactness and low power advantages of the SOA, but in addition it is passive and polarization independent.

5.1 Operation principle

As discussed in the previous sections, the nonlinear VCSG can be designed to have an inverse saturable absorber characteristic (i.e. high reflectivity at low input energy and low reflectivity at high input energy) for input energy values below the IM energy (see for instance Fig. 4 (right)). For this impedance-detuned design, when low input energies are used, ranging between zero and IM energy point, the gate reflectivity decreases with increasing energy. By exploiting the nonlinear characteristic at low energy of an impedance detuned VCSG, it is then possible to extract short return-to-zero (RZ) pulses synchronous with the leading edge of an incoming non-return-to-zero (NRZ) optical pulse, as explained in the following. Before the pulse arrival, the absorption in the MQWs is unsaturated and the gate is in the high-reflectivity state. Thus, when an optical NRZ pulse with appropriate peak power enters the gate, the low energy leading edge of the pulse is back reflected from the gate, whereas the following part of the pulse rapidly biases the gate in the IM condition and is strongly suppressed. This effect represents the basic principle we exploited to realize AO-HE and AO-SPE for optical packets with PPC optical headers.

5.2 Device modelling

A VCSG, working at its resonant wavelength, can be modeled as a two-level system with a single time constant, τ_s, which is the recovery time. The reflected output power $P_{ref}(t)$ is directly related to the input signal $P_{in}(t)$ as shown in (2); the absorption coefficient $\alpha(t)$ is time- and input power-dependent. If the round-trip time of the cavity is much lower than the time-scale associated with input power variations, as in most practical applications, the time dependence of the absorption can be described using the following nonlinear rate equation (Kartner et al., 1996):

$$\frac{\partial\alpha(t)}{\partial t}=\frac{\alpha_0-\alpha(t)}{\tau_s}-\frac{\xi(t)P_{in}(t)}{E_{sat}}\alpha(t) \quad . \tag{12}$$

Where the ξ parameter describes the ratio between the energies of the optical field within the cavity and the input optical fields and accounts for the FP resonant effects. At resonance, its value is given by (Brovelli et al., 1995):

$$\xi=\frac{1-Rt}{(1-\sqrt{R_tR_b}\exp[-\alpha d])^2} \, . \tag{13}$$

In a weakly saturated absorption regime, small variations of α do not affect the ξ parameter, which can be considered constant, and (12) has an analytical solution in the form:

$$\alpha(t)=\alpha_0\exp\left[-\frac{1}{\tau_s}\int_0^t\left(1+\frac{P(\tau)\tau_s}{E_{sat}}\right)d\tau\right]\cdot\left(1+\frac{1}{\tau_s}\int_0^t\exp\left[\frac{1}{\tau_s}\int_0^t\left(1+\frac{P(\tau)\tau_s}{E_{sat}}\right)d\tau\right]\right) . \tag{14}$$

where *P(t)* is the optical internal power. In the strongly saturated absorption regime, the previous approximation quickly fails, and can be used only to obtain a rough prediction for device dynamics; Numerical methods have to be used in order to obtain an accurate description for this case.

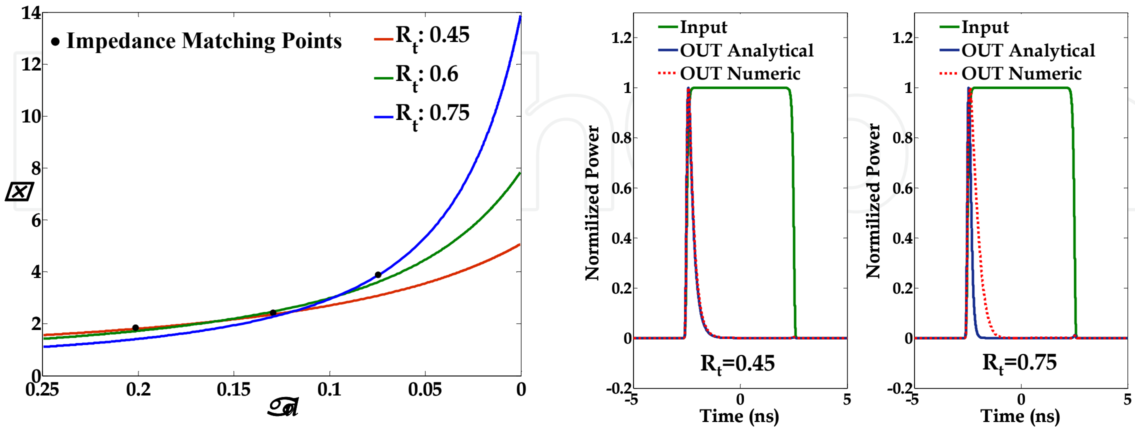

Fig. 10. Left: ξ as a function of the product *ad* for three different R_t values. IM conditions are indicated using black dots. Right: Numerical model vs. analytical solutions when an optical gate is used as input signal, for two different values of R_t. Other parameters: $\alpha_0 d$ = 0.25, E_{sat} = 1.5 pJ, τ_s = 0.5 ns.

In order to better understand the analytical approximation, ξ is plotted in Fig. 10 (left) as a function of the product αd for three different R_t values. In the same picture IM conditions are highlighted. For the proposed application, when a gate pulse is launched through the device, the αd product varies between its minimum and the IM point. At the same time, the ξ parameter exhibits a small variation, that increases as R_t gets higher. Thus, one pulse is generated by applying an optical gate to the VCSG. Fig. 10 (right) illustrates this situation, calculated using both numerical integration and analytical solution for two different values of the top mirror reflectivity. As discussed, the analytical solution diverges from the numerical one as the value of R_t is increased.

5.3 All-Optical header extraction with VCSG

The experimental set-up that that was employed for demonstrating AO-HE with optical packets encompassing a PPC header section is shown in Fig. 11. The CW laser source, matching the VCSG's resonant wavelength, was modulated by an amplitude modulator to produce the data packets. The packet format is also shown in the same figure (bottom). The header section consisted of two NRZ pulses at 2.5 Gbit/s (label A), separated by a sequence of alternating '0' and '1' bits (label B) at the same bit rate as the data payload (12 Gb/s), with the exception of a sequence of '0s' (label C) placed in front of the second header pulse. The 1.2 ns long sequence of '0s' was introduced to ensure complete recovery of absorption before the second header pulse entered the VCSG. The header was uniquely defined by the position of the second pulse (Calabretta et al., 2004). The payload was Manchester encoded to guarantee that the average signal power was constant, regardless of the specific bit pattern. The guard time between the packets was 1.2 ns.

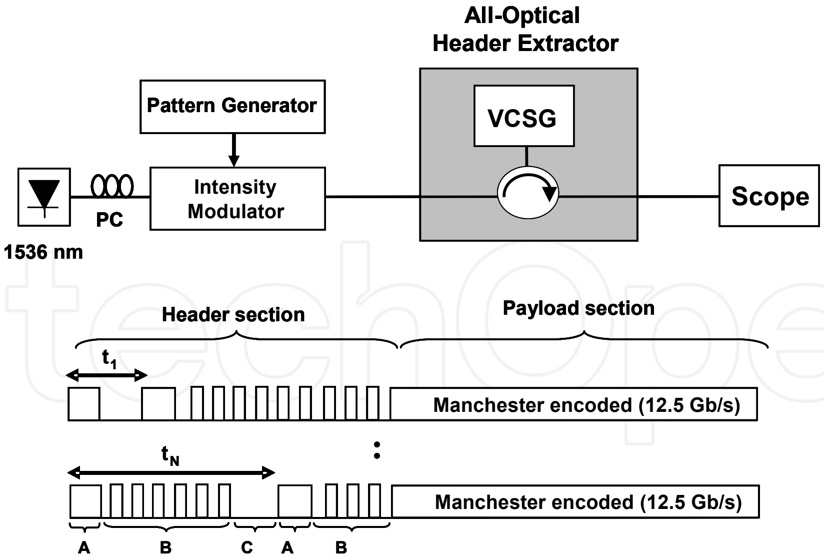

Fig. 11. The set-up and format of the packets used in the AO-HE experiment.

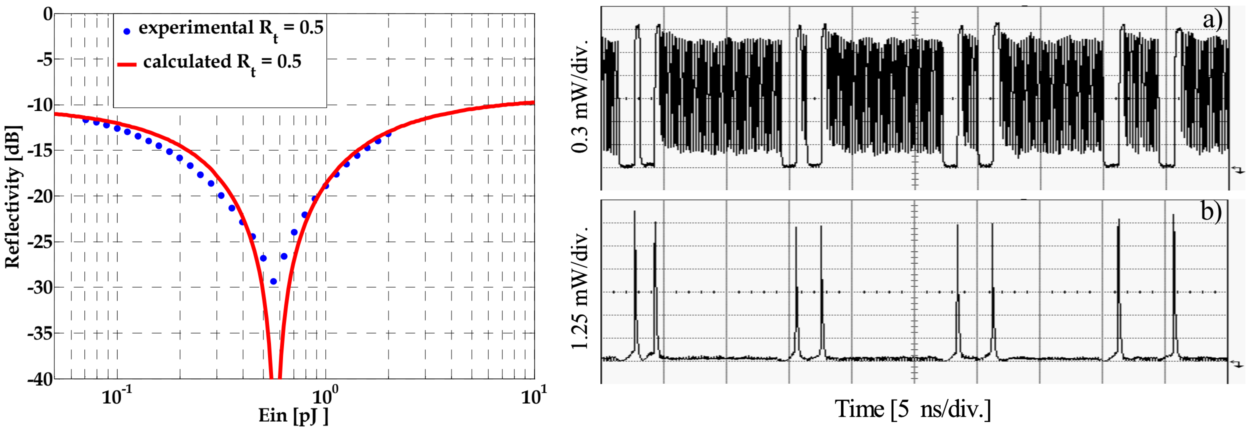

Fig. 12. Left: measured static VCSG nonlinear reflectivity (dots) and fitting with theoretical model (continuous). Right: Experimental results. a): Input data packets. b): Extracted headers at VCSG output

It should be noted that the payload data rate is not limited by the VCSG, and could be extended to higher data rates, provided that the absorber recovery time is sufficiently longer than the bit period. Indeed, the only limitation is that the absorber recovery time should be faster than the guard time between packets and slower than the data period in the payload. It is then expected that even shorter packet guard times would be sufficient at data rates exceeding 12.5 Gb/s. Fig 12 (left) reveals the measurement of the static nonlinear reflectivity of the VCSG at the resonant wavelength. The impedance matching was achieved for a pulse energy of ~0.5 pJ, where the reflectivity is 18 dB lower than the reflectivity for low energy signals. This value sets the limit *CR* of the device in the dynamic operation. A static model, obtained by inserting the steady-state solution $d\alpha/dt=0$ of (12) in (2), was used to fit the experimental data and extract the absorber parameters. The fitting, also shown in the figure, corresponds to $E_{sat} = 1.3$ pJ, $\alpha_0 d = 0.25$, and non-saturable round-trip losses $\alpha_{ns}d = 0.08$. The value of τ_s was determined with a pump-probe measurement to be ~500 ps. In the experiment, four optical packets with different headers (see Fig. 12a, right) were sent to the

VCSG. The output of the VCSG is shown in Fig 12b (right), clearly revealing the two extracted pulses synchronous with the leading edges of the two header pulses in each packet. The payloads immediately following the pulses in the second header were almost completely suppressed, since they encountered the VCSG in the impedance matched state. The *CR* between the two pulses and the suppressed payload was higher than 14 dB for each extracted header pulse. The average input power at the VCSG was about 0 dBm. The gate efficiency (the ratio between input header power and extracted pulse peak power) was calculated to be ~6 %. The effect of top mirror reflectivity on the gate reflectivity at low-energy can be seen in Fig. 7 (right), showing that higher R_t values result in higher values of the low-energy reflectivity, which in turns would increase the efficiency of the VCSG-based AO-HE. However, from the static characteristics it can be also seen that the energy required for matching the impedance of the gate would also increase with R_t.

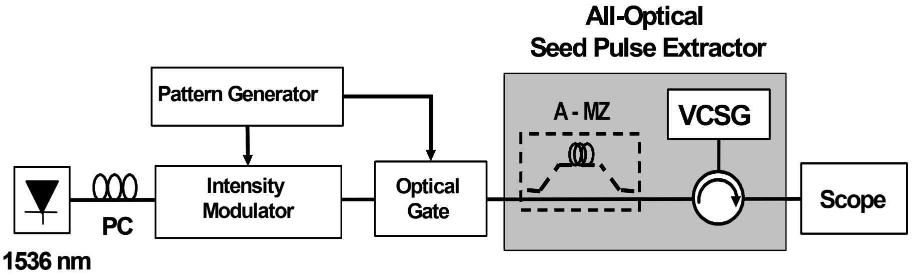

Fig. 13. Experimental setup for the AO-SPE with VCSG.

5.4 All-Optical Seed Pulse Extraction with VCSG

In optical packet switched networks, phase alignment between each packet at an optical packet switching node is required in order to perform packet routing (Sakamoto et al, 2002). Self-synchronization is one of the methods used to achieve packet phase alignment. With self-synchronization, a single pulse seed synchronous with the beginning of the packet is selected from an incoming data pattern. The seed pulse can be used for generating a local clock for packet synchronization, and for driving the subsequent node subsystems (Xia et al., 1999; Huanget al., 2005). An all-optical seed pulse extractor based on self-induced nonlinear reflectivity in a VCSG is described in this section. The experimental set-up that was employed is shown in Fig. 13. Again, the CW laser source at 1536 nm, matching the resonant wavelength of the VCSG, was modulated by an intensity modulator to produce data packets. The modulator was driven by a pattern generator at 12.5 Gbit/s. The optical gate was used to provide an appropriate guard time between the packets for complete recovery of the MQWs absorption. The packet format was the same as in Fig 11. With respect to the previous experiment, an asymmetric Mach-Zehnder (A-MZ) interferometer was inserted, having a delay between the two arms equal to the sequence of "0" bits before the second header (label C); the delay was set to be ~1.2 ns. The output of the A-MZ consisted of the sum of the data packet and its delayed replica. In this way the '0s' sequence was no longer present at the VCSG input. Thus, only the leading edge of the first NRZ header produced a pulse synchronized with the beginning of the packet, while the rest of the packet was suppressed because it experienced IM reflectivity. Fig. 14 shows the input/output waveforms of the AO-SPE. The measured output signal CR was 12 dB.

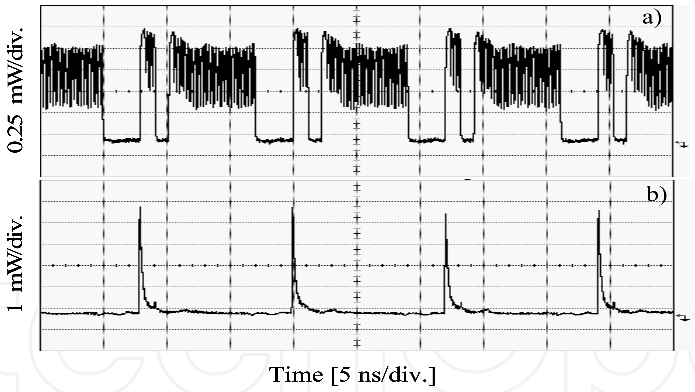

Fig. 14. VCSG input (a), and output (b) traces for the experiment of Fig. 13.

6. All-Optical NAND/NOR Logic Gates based on VCSG

Logical operations performed in the optical domain are required to enable ultra-fast signal processing in all-optical networks. All-optical logic gates can be used to perform many functions in optical packet-switched network. These functions include header recognition and/or modification, packet contention handling, data encoding/decoding, and realization of half- and full-adders. Up to now, semiconductor SAs based on MQWs have been only used to implement ultra-fast *AND* functions (Takahashi et al. 1996, Loka et Smith, 1998), due to their typical nonlinear behaviour, exhibiting low throughput at low powers and high throughput at high powers. An inverse saturable absorption mechanism would allow the use of VCSGs to realize *NAND/NOR* logical operations (Porzi et al., 2008).These functions are particularly important because any logical operations can be realized using only *NAND* or *NOR* operators.

6.1 Operation principle and device optimization

From (6) and (2) it can be seen that, if the VCSG's top mirror reflectivity R_t satisfies the condition:

$$R_t = R_b e^{-2\alpha_{ns} d} , \tag{15}$$

the minimum reflectivity (i.e. the IM) is achieved at high input energy (E>> E_{sat}), as can be easily verified from (5) and (2). In this case, at the resonant wavelength, the VCSG exhibits an inverse saturable absorber characteristic. The simulated behaviour of a VCSG designed to meet the IM condition at high input energies is shown in Fig 15 (left).

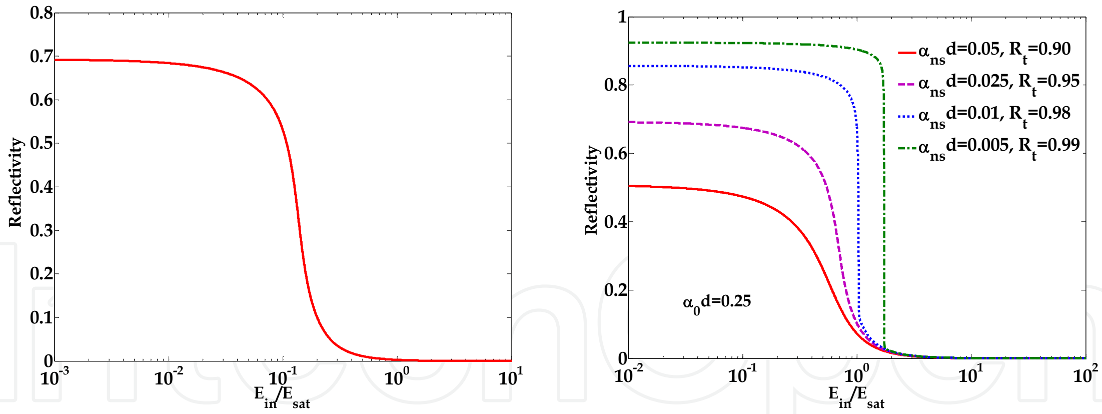

Fig 15. Left: Simulated nonlinear reflectivity at resonance wavelength for a VCSG designed to satisfy the IM condition for totally saturated absorption. Simulation parameters: $\alpha_0 d=0.25$, $\alpha_{ns}d=0.025$, $R_b=1$, and $R_t=0.95$. Right: different plots corresponding to different values of $\alpha_{ns}d$.

In order to implement effective *NAND/NOR* logical operations, it would be desirable to have a step-like characteristic with a sharp transition between the *ON* and the *OFF* states. The well-known phenomenon of field enhancement (at resonance) in a Fabry-Pérot cavity can be exploited to enhance the nonlinear reflectivity change and obtain a steep *ON/OFF* transition. At resonance, the intensity distribution inside the structure can be much higher (or lower) than the input energy, depending on the working conditions. The ratio between the energy inside the cavity and the energy incident on it at the resonant wavelength is given by the parameter ξ, introduced in eq (13). Large changes of ξ for small changes of the input energy enable steep transitions between the *ON* and *OFF* states to be realized. Since the *OFF* state corresponds to the case in which only the non-saturable losses are present in the cavity, the internal energy enhancement factor ξ should exhibit a large increase when α approaches α_{ns}. For $E>>E_{sat}$,

$$\xi_{E\to\infty} = \frac{(1-R_t)}{\left(1-\sqrt{R_t R_b}\, e^{-2\alpha_{ns}d}\right)^2} \tag{16}$$

If the top mirror is optimized for impedance matching at high powers, then the previous expression becomes:

$$\xi_{E\to\infty}^{IM} = \frac{1}{1-R_b e^{-2\alpha_{ns}d}} \tag{17}$$

And, for R_b=1 and $\alpha_{ns}\to 0$ then $\xi\to\infty$. Indeed, in the limit of $\alpha_{ns}\to 0$ and $\alpha_0\to 0$ it can be seen from eq. (15) that we are dealing with the case of an ideal, lossless, symmetric Fabry-Pérot resonator, which has infinite finesse. In practical cases, small values of α_{ns} enable to high values of the internal field enhancement factor to be achieved when the absorber is saturated. In this way, the dynamic input energy range for which the gate changes its operating state is also reduced, giving rise to a step-like characteristic as a function of the input energy. Fig 15 (right) reveals the effect of decreasing α_{ns} (for a fixed value of α_0), on the nonlinear reflectivity characteristic measured at the resonant wavelength. The corresponding values of R_t (given by (15)) are also shown. It can be seen that very sharp transitions correspond to very high values of R_t. Furthermore, in the high-finesse limit, optical bistability may appear, preventing correct operation of the device. The operation principle of the NAND/NOR gates is briefly explained in the following. If a CW probe field is tuned at the cavity resonance, with optical power P_{pb} partially saturating the MQWs absorption, it can initially experience a high value of reflectivity. If two pump signals are applied to the device, and if the single pump power P_{pmp} is not enough to switch the gate in the *OFF* state, whereas twice the pump power is, the reflected probe power represents the *NOR* of the input pump signals. On the other hand, if the power of a single pump signal is enough to turn the gate in the *OFF* state, *NAND* between the two pumps is retrieved by filtering the reflected probe power.

6.2 Simulation results

In order to realize *NAND/NOR* operation with the reverse SA characteristic, a pump-probe configuration is required in which two data pump beams would affect the reflectivity experienced by the probe signal, providing the result of the desired logical operations. For practical applications, where transparency of the device with respect to input pump signals is desirable, only the probe signal is tuned at a cavity resonance, whereas the wavelength of the two pumps could be tuned away from resonance. A spectral analysis of the gate operation is then required. The dependence on the single-pass phase for the reflectivity of the VCSG is given by (1), whereas the wavelength-dependent internal energy enhancement factor is given by:

$$\xi = \frac{\left(1-R_t\right)}{\left[1-\sqrt{R_t}\sqrt{R_b}\exp(-\alpha d)\right]^2 + 4\sqrt{R_t}\sqrt{R_b}\exp(-\alpha d)\sin^2(\phi_{sp})} \tag{18}$$

By using eqs (1) and (20), and the power dependence of α expressed by eq. (4), it is possible to calculate the spectral reflectivity of the VCSG for different values of both the input pump and probe energy and wavelength. The calculated spectral reflectivity of the nonlinear gate under different input power conditions is shown in Fig. 16 (left) and Fig. 16 (right) for the cases of *NAND* and *NOR* operation, respectively. In the *NAND* case, for suitable values of the input probe and pump powers, it can be seen that the reflectivity is always high when either the probe field or the probe and a single pump pulse are applied to the gate. On the other hand, if twice the pump power is applied to the gate, the reflectivity at the resonant wavelength is drastically reduced. In the *NOR* case, one single pump pulse contains enough energy to turn the gate to the *OFF* state. It can also be seen that the resonance width changes drastically when passing from the *ON* to the *OFF* state. The resonance width in the *OFF* state is inversely proportional to the steepness of the nonlinear characteristic, thus a trade-off between resonance bandwidth and the *ON/OFF* contrast ratio has to be considered in designing the device. Except for the pump powers, the parameters used to calculate the spectral reflectivity were the same for the examples shown in the two figures. Thus, for a suitable bias level of the probe beam, the two functions can be obtained in the same device by changing the pump power. In an alternative arrangement, the biasing probe power can be changed, while keeping the pump power constant, to switch between the two logical operations.

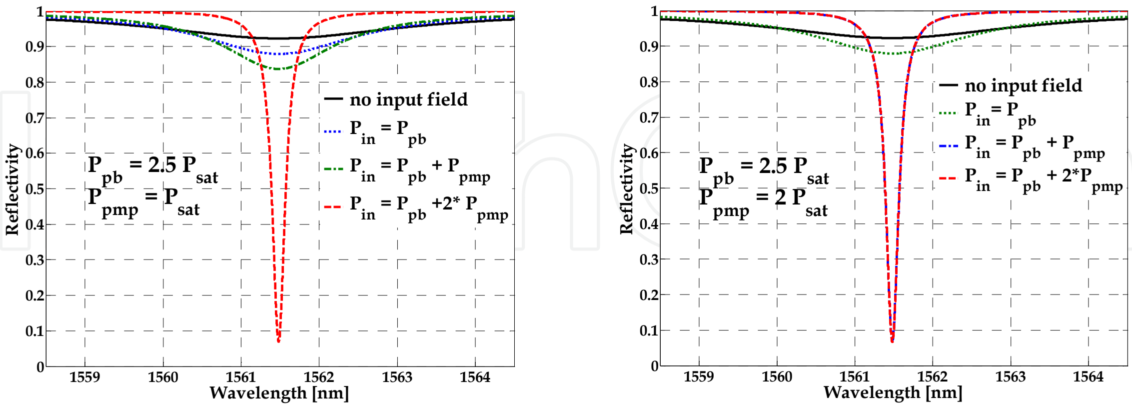

Fig. 16. Left: spectral reflectivity for different input powers for *NAND* gate. Right: spectral reflectivity for different input powers for *NOR* gate. Other simulation parameters: $\alpha_0 d$=0.25, $\alpha_{ns} d$=0.005, and 1 nm pump detuning from resonance.

6.3 Effects of cavity parameters

In a previous section it has been shown that low values of $\alpha_{ns} d$ are desirable for good operation. Here, also the effects of $\alpha_0 d$ on the device performances are investigated. In our simulations we first calculated the nonlinear reflectivity at the resonant wavelength to assess an appropriate value for the input probe power, and then we evaluated the reflectivity variation experienced by the probe field as a function of pump power, for a given pump detuning from resonance. The simulations were performed by means of the nonlinear spectral model previously introduced. In the simulations, the value of R_b was assumed to be 100% and that of R_t was set to the value satisfying the condition given by (15). Pump detuning from resonance was 1 nm. The results of the simulations are shown in Fig 17. Each pair of figures represents the nonlinear reflectivity at resonance, induced by the probe (upper plots) and the pump field (lower plots), for a fixed value of probe power. Each figure corresponds to a fixed value of $\alpha_0 d$ for three different values of $\alpha_{ns} d$. As previously discussed, the steepest characteristic is obtained for the smallest value of $\alpha_{ns} d$. However, very small values of the non-saturable losses $\alpha_{ns} d$ also lead to unpractical values of top mirror reflectivity (> 0.99). Furthermore, as will be clear later on in this section, this situation also makes bistability more likely to occur. On the other hand, increasing $\alpha_0 d$ leads to good extinction ratio values even in the presence of moderate values of $\alpha_{ns} d$, and increases the gate efficiency. However, high values of $\alpha_0 d$ could be difficult to obtain in practice, and would also increase the saturation power (hence preventing low-power operation) and increase the non-saturable losses. A trade-off between ideal device parameters and practical implementation should hence be considered. In the following, only small or moderate values of $\alpha_0 d$ will be considered, which are more likely to be realized in a practical device with low values of non-saturable losses. The results we have obtained can be improved by using higher values of $\alpha_0 d$.

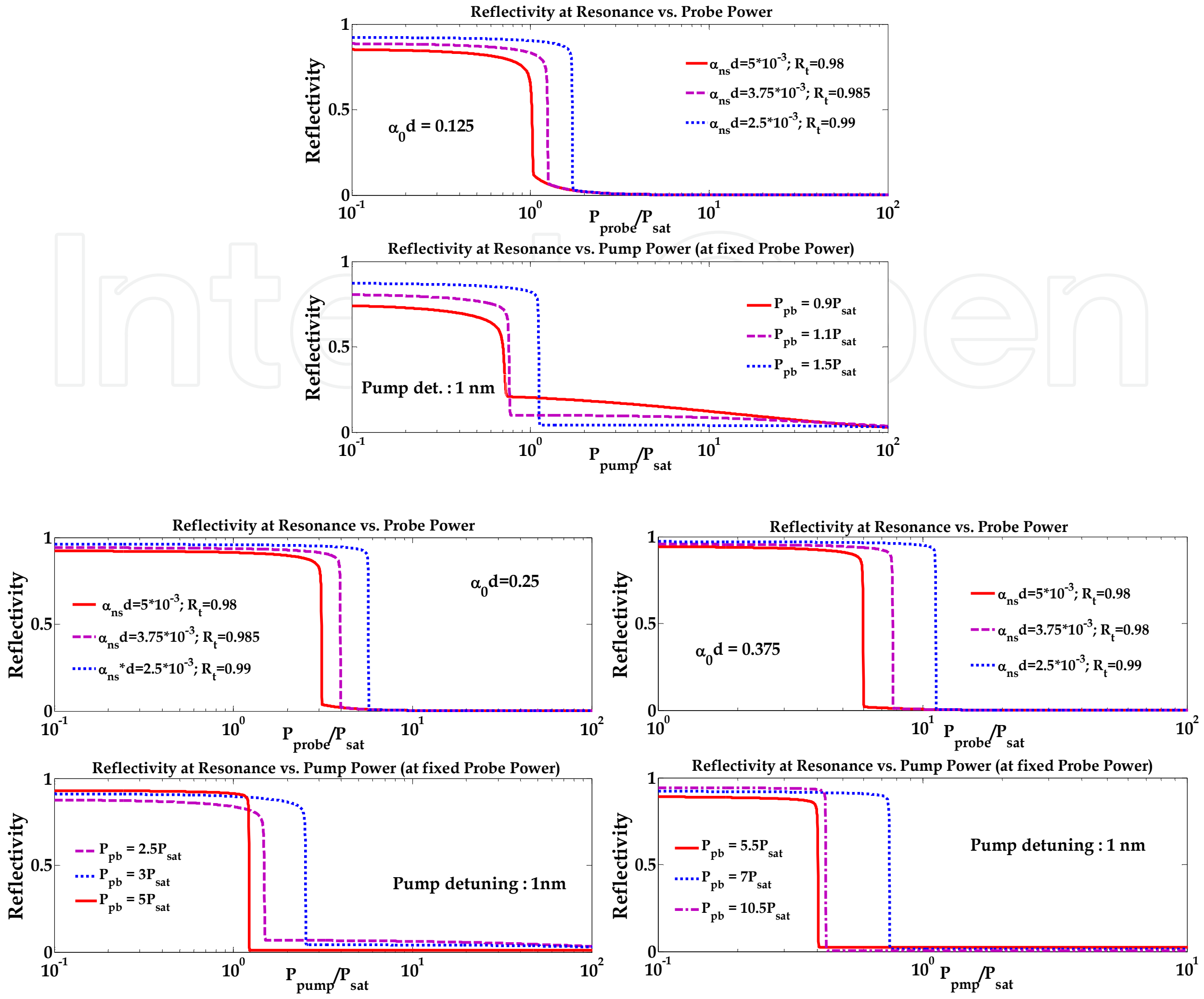

Fig. 17. Effect of $\alpha_{ns}d$ parameter for three different values of $\alpha_0 d$.

6.4 Bistability Analysis

Under particular conditions, bistable operation may appear in the device, meaning that when the pump field is switched off the device could remain in the OFF state rather than going back to its initial ON state. Although it could be useful in other system applications, this situation should be avoided for logical *NAND/NOR* operations. An analysis of bistability can be made by using a procedure similar to that described in (Garmire, 1989), in which the nonlinear effect was only associated with refractive index changes, rather than absorption. Here, for the sake of simplicity, we neglect the nonlinear index change (assumed to be small with respect to the effect of absorption), and consider only the effects of absorption saturation. The input-reflected (I_{in}-I_{ref}) light characteristic at resonance for different values of $\alpha_{ns}d$ and fixed $\alpha_0 d$ are shown in Fig. 18 (left). It can be seen that for the lower value of $\alpha_{ns}d$, the device exhibits bistable behaviour. Thus, bistability sets a limit on the ideal minimum value of internal non-saturable losses.

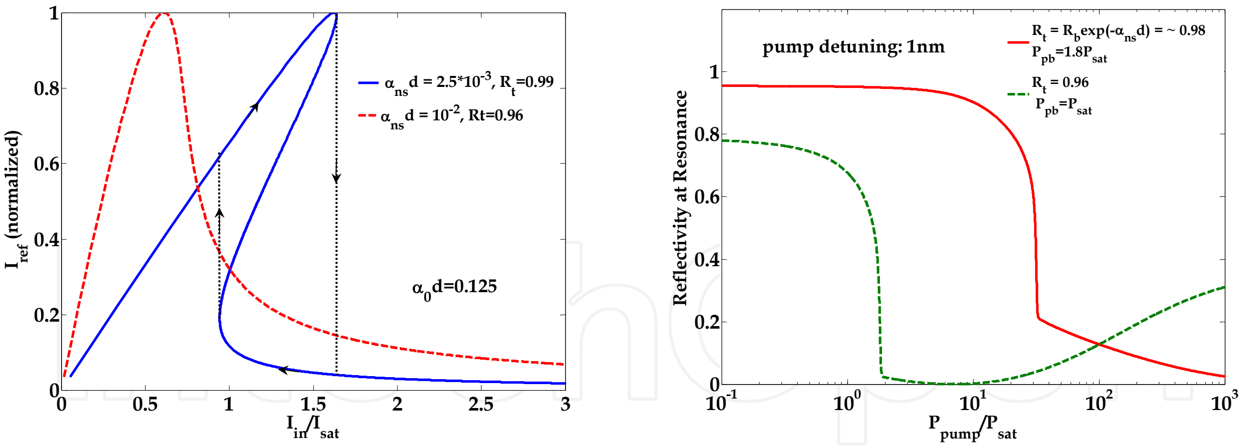

Fig. 18. Left: I_{in}-I_{ref} characteristics of the nonlinear VCSG showing bistable (solid line) and non-bistable (dashed line) behavior for two different values of $\alpha_{ns}d$, and fixed $\alpha_0 d$. Right: Nonlinear reflectivity vs. P_{pmp} for a probe power outside the hysteresis region for $R_t=exp(-a_{ns}d)$ (solid line), and $R_t=0.97exp(-a_{ns}d)$ (dashed line).

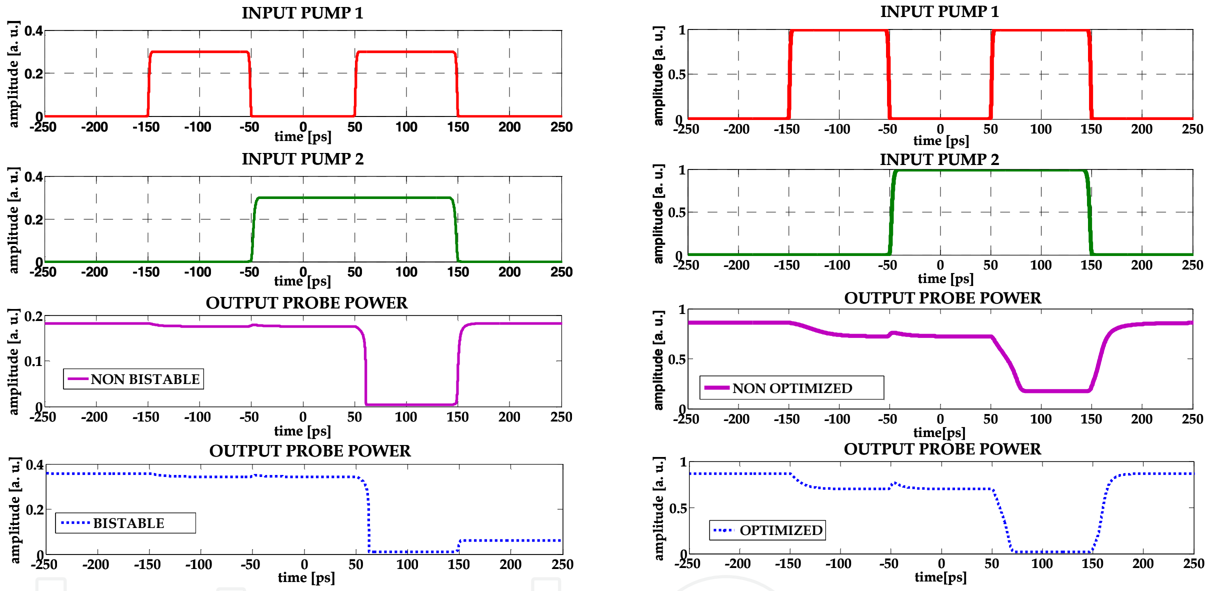

Fig. 19. Left: dynamic NAND operation with NRZ pulses at 10 Gb/s for pump and probe signals tuned at two different resonances ($\alpha_{ns}d$= 0.005, $\alpha_0 d$ = 0.25, $P_{pb}=P_{sat}$); the output probe power for non bistable (solid line) and bistable (dashed lines) cases, are shown. Right: dynamic *NAND* operation relative to the static characteristics of Fig 18; output probe power for non optimized (solid line) and optimized (dashed lines) cases, are shown

Occurrence of bistability can be avoided in two ways, as explained below. The first one is to design a cavity which is inherently non-bistable, like the one associated with the dashed curve in the Fig. 18 (left). The second one is to bias the gate with a proper value of input probe power which lies outside the hysteresis region of the solid curve in Fig. 18 (left). Both these solutions affect the quality of the output signal. As an example, Fig. 18 (right, solid line), shows the reflectivity at a resonance as a function of P_{pmp} for a probe power sufficiently low to avoid bistability, a pump wavelength detuned 1 nm apart from the resonance, and a top mirror reflectivity $R_t=exp(-a_{ns}d)$. It can be seen that the smooth slope of the reflectivity in the proximity of highly saturated absorption (high pump power) leads to a poor output probe *CR*. This suggests an improved operation by matching the gate impedance for a value of absorption corresponding to the applied pump power. That is, a top mirror reflectivity slightly lower than $exp(-a_{ns}d)$. The effect is shown in Figure 18 (right, dashed line), for a top mirror reflectivity R_t= 96%, corresponding to $0.97\cdot exp(-a_{ns}d)$. The increased *CR* is attained at the expenses of slightly reduced gate efficiency. Lowering the top mirror reflectivity also helps to further prevent bistability, by reducing cavity finesse. The required switching power is reduced too.

6.5 Dynamic Operation

The dynamic model expressed by (12) can be extended to take into account pump and probe optical fields with a generic detuning from resonance:

$$\begin{aligned}\frac{d\alpha}{dt}=\frac{\alpha_0-\alpha}{\tau_s}&-\frac{\left(1-R_t\right)\cdot P_{pb}\cdot\alpha}{E_{sat}\left[\left(1-\sqrt{R_t}\cdot\sqrt{R_b}\cdot e^{-(\alpha+\alpha_{ns})\cdot d}\right)^2+4\sqrt{R_t}\cdot\sqrt{R_b}e^{-(\alpha+\alpha_{ns})\cdot d}\sin^2\left(\phi_{pb}\right)\right]}\\&-\frac{\left(1-R_t\right)\cdot P_{pmp}\cdot\alpha}{E_{sat}\left[\left(1-\sqrt{R_t}\cdot\sqrt{R_b}\cdot e^{-(\alpha+\alpha_{ns})\cdot d}\right)^2+4\sqrt{R_t}\cdot\sqrt{R_b}e^{-(\alpha+\alpha_{ns})\cdot d}\sin^2\left(\phi_{pmp}\right)\right]}\end{aligned}\tag{19}$$

where ϕ_{pb} and ϕ_{pmp} are the single-pass phases associated with probe and pump wavelengths, respectively; and τ_s is the carrier recombination time in the MQWs. In the following we have assumed τ_s=5 ps. Let us first consider the simple case in which both the pump and the probe fields are tuned in proximity of two cavity resonances. This case correspond to an optimal condition in which a steep transition can be preserved, even for a probe biasing power away from the nonlinear characteristic transition edge to prevent bistability, thanks to the enhancement factor experienced by the pump field in the resonator. For this situation, the results of dynamic simulations are shown in Fig. 19 (right), for the case of NRZ input pump data at 10 Gb/s. For comparison, the dynamic behavior in the case of bistable operation is also shown in the figure (dashed line). However, in practical applications transparency of the operation to the data wavelength is a desirable condition. As previously discussed, hysteresis can be avoided by setting the bias power not too close to the transition edge. Fig. 19 (left, solid line) shows dynamic *NAND* operation for the case relative to Fig. 18 (right, solid line). As expected, although the operation is preserved, the *CR* of the output signal is degraded due to a non ideal characteristic of the gate. The case relative to the static analysis of Fig. 18 (right, dashed lines), where the gate impedance was matched for a partially saturated absorption coefficient corresponding to the value inferred by two data pulses, was also investigated in the dynamic simulation, and the results are shown in Fig. 19 (right, dashed line). It can be seen that *NAND* operation with high *CR* for the filtered probe light can be obtained for this case. Implementation of *NOR* operation is straightforward. In this case there is less constraint on the steepness of the probe nonlinear reflectivity characteristic induced by the pump field. For *NOR* operation, indeed even a relatively smooth characteristic can be tolerated, provided that each pump pulse has enough power to switch the gate to the *OFF* state. However, low-power operation is always desirable, and we can take advantage of the previous considerations to implement efficient, low-power, *NOR* gate with reverse-SA VCSG. As an example, Fig. 20 shows *NOR* operation of the VCSG relative to the case of Fig 18 (right, dashed line) with a pump power ranging within the low-reflectivity region of the figure.

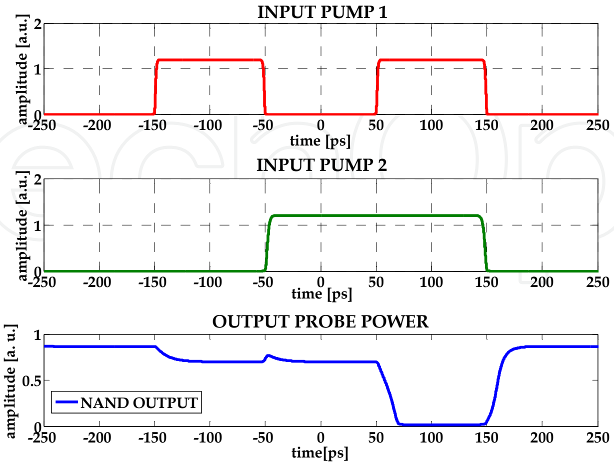

Fig. 20. *NOR* operation with VCSG parameters as in Fig 18 (right, dashed line).

7. Conclusion

In this chapter we have given detailed information on the design, fabrication, and operation of VCSGs based on saturable absorption in semiconductor quantum-wells. Different applications for optical communication subsystems have been discussed. These applications include, but are not limited to, wavelength conversion/optical gating, advanced signal processing functionalities for all-optical networks, and all-optical logical operations. The versatility in tailoring the nonlinear characteristics of the VCSG for a particular application has been discussed using numerical and analytical models.

8. References

Agrawal G. P. (2002), *Fiber-Optic Communication Systems 3rd Ed.*, John Wiley & Sons Inc, 0471215716, New York

Akiyama, T.; Tsuchiya, M.; Kamiya, T. (1998). Sub-pJ operation of broadband asymmetric Fabry-Pérot all-optical gate with coupled cavity structure. *Applied Physics Letters*, Vol. 72, No. 13, (Mar. 1998) pp. 1545-1547, 0003-6951

Brackett C. A.; Acampora A. S.; Sweitzer J.; Tangonan G.; Smith M. T.; Lennon W.; Wang K.-C.; Hobbs R. H. (1993). A scalable multiwavelength multihop optical network: A proposal for research on all-optical networks. *Journal of Lightwave Technology*, Vol. 11, No. 5/6 (May/June 1993) pp. 736-753, 0733-8724

Brovelli L.; Keller U.; and Chiu T. (1995). Design and operation of antiresonant Fabry-Pérot saturable semiconductor absorbers for mode-locked solid-state lasers. *Journal of the Optical Society of America B-Optical Physics*, Vol. 12, No. 2, (Feb. 1995) pp. 311-320, 0740-3224

Burr E. P.; Pantouvaki M.; Seeds A. J.; Gwilliam R. M.; Pinches S. M.; Button C. C. (2003). Wavelength conversion of 1.53-µm-wavelength picosecond pulses in an ion-implanted multiple-quantum-well all-optical switch. *Optics letters*, Vol. 28, No. 6 (Mar. 2003) pp. 483-485, 0146-9592

Calabretta N.; Liu Y.; Waardt D. H.; Hill M. T.; Khoe G. D.; Dorren H. J. S. (2001). Multiple-output all-optical header processing technique based on two-pulse correlation principle. *Electronics Letters*, Vol. 37, No. 20, (Sept 2001) pp. 1238–1240, 0013-5194

Calabretta N.; Liu Y.; Huijskens F. M.; Hill M. T.; De Waardt H.; Khoe G. D.; Dorren H. J. S. (2004). Optical signal processing based on self-induced polarization rotation in a semiconductor optical amplifier. *Journal Of Lightwave Technology*, Vol. 22, No. 2, (Feb. 2004) pp. 372-381, 0733-8724

Delpon E. L.; Oudar J. L.; Bouché N.; Raj R.; Shen A.; Stelmakh N.; Lourtioz J. M. (1998). Ultrafast excitonic saturable absorption in ion-implanted InGaAs/InAlAs multiple quantum wells. *Appied Physics Leters*, Vol. 72, No. 7, (Feb. 1998) pp.759–761, 0003-6951

Garmire E. (1998). Criteria for optical bistability in a lossy saturating Fabry-Pérot. *Journal of Quantum Electronics*, Vol. 25, No. 3, (March 1989) pp. 289 – 295, 0018-9197

Huang X.; Ye P.; Zahng M.; Wang L. (2005). A Novel Self-Synchronization Scheme for All-optical Packet Networks. *IEEE Photonics Technology Letters*, Vol. 17, No. 3, (March. 2005) pp. 645-647, 1041-1135

Isomaki, A.; Vainionpaa, A. M.; Lyytikainen, J.; Okhotnikov, O. G. (2003). Semiconductor mirror for optical noise suppression and dynamic dispersion compensation. *Journal of Quantum Electronics,* Vol. 39, No. 11, (Nov. 2003) pp. 1481-1485, 0018-9197

Kartner F. X., Jung I. D., Keller U. (1996) Soliton Mode-Locking with Saturable Absorbers, *Journal Of Selected Topics in Quantum Electronics*, Vol. 2, No. 3, (Sept. 1996.) pp. 540-556, 1077-260X

Keller, U.; Weingarten, K. J.; Kartner, F. X.; Kopf, D.; Braun, B.; Jung, I. D.; Fluck, R.; Honninger, C.; Matuschek, N.; Aus der Au, J. (1996). Semiconductor saturable absorber mirrors (SESAM's) for femtosecond to nanosecond pulse generation in solid-state lasers. *Selected Topics in Quantum Electronics,* Vol. 2, No. 3, (Sep. 1996) pp. 435-453 1077-260X

Loka H. S.; Smith P. W. E. (1998). Ultrafast All-Optical Switching in an Asymmetric Fabry–Pérot Device Using Low-Temperature-Grown GaAs. *IEEE Photonics Technology Letters*, vol. 10, No. 12, (Dec. 1998) pp. 269-271, 1733-1735, 1041-1135

Massoubre D.; Fatome J.; Pitois S.; Decobert J.; Landreau J.; Millot G.; and Oudar J. L. (2006). All-aptical exctintion ratio enhancement of a 160 GHz pulse train using a saturable absorber vertical microcavity. *Optics letters*, Vol. 31, no. 4, (Feb. 2006) pp. 537-539, 0146-9592

Porzi C.; Isomaki A., Guina M.; and Okothnikov O. (2005). Impedance-detuned high-contrast vertical cavity semiconductor switch, *Proceeding OFC 2005.,* pp. OThM5, 1-55752-783-0, Anaheim Convention Center, Anaheim, California

Porzi C.; Bogoni A.; Poti L.; Guina M.; and Okhotnikov O. (2006). Characterization and operation of vertical cavity semiconductor all-optical broadband wavelength converter, *Proceeding SPIE Integrated Optics, Silicon Photonics, and Photonic Integrated Circuits*, pp. Z1830-Z1830, 0-8194-6239-X, Strasbourg, France

Porzi C.; Calabretta N.; Guina M.; Okhotnikov O.; Bogoni A.; and Potì L. (2007). All-Optical Processing for Pulse Position Coded Header in Packet Switched Optical Networks Using Vertical Cavity Semiconductor Gates. *Selected Topics in Quantum Electronics,* Vol. 13, No. 5, (Sept.-Oct. 2007) pp 1579–1588, 1077-260X

Porzi C.; Guina M. ; Bogoni A. ; Poti, L. (2008). All-Optical nand/nor Logic Gates Based on Semiconductor Saturable Absorber Etalons. *Selected Topics in Quantum Electronics,* Vol. 14, No. 3, (May-June 2008) pp 927–937, 1077-260X

Siegman A. E. (1986), *Lasers*, University Science, 0935702113, Mill Valley, California

Sakamoto T.; Okada A.; Hirayama M.; Sakai Y.; Moriwaki O.; Ogawa I.; Sato R.; Noguchi K.; Matsuoka M. (2002). Demonstration of an optical packet synchronizer for an optical packet switch. *Proceeding OFC 2002*, pp. 762-763, 1-5572-700-8, Anaheim Convention Center, Anaheim, California

Takahashi R.; Kawamura Y.; Iwamura H. (1996). Ultrafast 1.55 mm all-optical switching using low-temperature-grown multiple quantum wells. *Applied. Phyics Letters*, Vol. 68, No. 2, (Jan. 1996) pp. 153–155, 0003-6951

Vegas Olmos J. J.; Tafur Monroy I.; Turkieveia J. P.; Liu Y.; Koonen A. M. (2006). Self-Controlled All-Optical Label and Payload Separator or Variable Length Burst in a Time-Serial IM/DPSK Scheme. *IEEE Photonics Technology Letters*, vol. 17, No. 8, (Aug. 2005) pp. 1692-1694, 1041-1135

Xia T. J.; Kao Y. H.; Liang Y.; Lou J. W.; Ahn K. H.; Boyraz O.; Nowak G. A.; Said A. A.; Slam M. N. (1999). Novel Self- Synchronization Scheme for High-Speed Packet TDM Networks. *IEEE Photonics Technology Letters*, vol. 11, No. 2, (Feb. 1999) pp. 269-271, 1041-1135

Xiang N.; Okhotnikov O.; Vainionpaa A.; Guina M.; Pessa M. (2001). Broadband semiconductor saturable absorber mirror at 1.55. *Electronics. Letters*, vol. 37, No. 6, (Mar. 2001) pp. 374-375, 0013-5194

Yan, R. H.; Simes, R. J.; Coldren, L. A. (1991). Surface-normal electroabsorption reflection modulators using asymmetric Fabry-Pérot structures. *IEEE Journal of Quantum Electronics,* Vol. 27, No. 7, (June 1991) pp. 1922 - 1931, 0018-9197

Semiconductor Technologies

Edited by Jan Grym

ISBN 978-953-307-080-3
Hard cover, 462 pages
Publisher InTech

Published in print edition April, 2010

Claudio Porzi, Mircea Guina, Nicola Calabretta, Antonella Bogoni and Luca Poti (2010). Applications of Saturable Absorption-based Nonlinear Vertical-Cavity Semiconductor Devices for All-Optical Signal Processing, Semiconductor Technologies, Jan Grym (Ed.), ISBN: 978-953-307-080-3, InTech, Available from: http://www.intechopen.com/books/semiconductor-technologies/applications-of-saturable-absorption-based-nonlinear-vertical-cavity-semiconductor-devices-for-all-o

InTech Europe
University Campus STeP Ri
Slavka Krautzeka 83/A
51000 Rijeka, Croatia
Phone: +385 (51) 770 447
Fax: +385 (51) 686 166
www.intechopen.com

InTech China
Unit 405, Office Block, Hotel Equatorial Shanghai
No.65, Yan An Road (West), Shanghai, 200040, China
中国上海市延安西路65号上海国际贵都大饭店办公楼405单元
Phone: +86-21-62489820
Fax: +86-21-62489821